Shaping trailing beams for beam loading via beam-induced-ionization injection at FACET

Lígia Diana Amorim[*,†] and Navid Vafaei-Najafabadi
Department of Physics and Astronomy, Stony Brook University, Stony Brook, New York 11794, USA

Claudio Emma, Christine I. Clarke, Selina Z. Green, Doug Storey, Glen White, Brendan O'Shea, Mark J. Hogan, and Vitaly Yakimenko
SLAC National Accelerator Laboratory, Menlo Park, California 94025, USA

Michael Litos
University of Colorado Boulder, Boulder, Colorado 80309, USA

Gaurav Raj, Olena Kononenko, Pablo San Miguel Claveria, and Sébastien Corde
LOA, ENSTA Paris, CNRS, Ecole Polytechnique, Institut Polytechnique de Paris, 91762 Palaiseau, France

Spencer Gessner
CERN, Geneva, 1211, Switzerland

Xinlu Xu, Ken Marsh, Chris E. Clayton, Chandrashekhar Joshi, and Warren B. Mori
University of California Los Angeles, Los Angeles, California 90095, USA

Erik Adli
University of Oslo, 0316 Oslo, Norway

(Received 16 August 2019; published 12 November 2019)

Recent progress in plasma based accelerator technology has demonstrated its ability to deliver high energy (GeV) beams in compact structures (centimeter to meter scale plasmas). Current developments of that technology are oriented toward producing beams with quality and energy spread comparable to those obtained using standard accelerating structures. In plasma based accelerators, the beam energy spread can be improved during the acceleration process through beam loading. To achieve optimum beam loading, the beam has to be shaped such that the superposition of its space charge fields and plasma fields result in a uniform accelerating field. In this work we show how beam-induced-ionization injection can be used to shape and inject a trailing beam suitable for beam loading. Our particle-in-cell numerical simulations done with OSIRIS show the ionization injection of a shaped 340 pC, 13 kA and 3 μm long electron beam accelerated to 900 MeV in less than 3 cm of plasma. The configurations considered numerically were based on the beams and plasmas that have been and will be available at the FACET facility.

DOI: 10.1103/PhysRevAccelBeams.22.111303

I. INTRODUCTION

Radio-frequency (rf) cavities have enabled critical advances in collider and free-electron-laser (FEL) applications of medicine, industry, and science [1,2]. Their accelerating fields are typically limited by vacuum breakdown to below tens of MeV/m [3,4]. In contrast, accelerator technology based on plasmas, which are not subject to breakdown, can sustain tens of GeV/m [5–7]. They can, in principle, accelerate particles to the same energy as rf cavities in a distance that is three orders of magnitude shorter. Plasma based accelerators (PBAs) are therefore ideal candidates for replacing rf cavities in future compact accelerator sources for collider and FEL applications. A PBA configuration proposed and studied for these applications operates in the blowout regime where a

[*]LDianaAmorim@lbl.gov
[†]Current address: Lawrence Berkeley National Laboratory, Berkeley, California 94702, USA.

driver, which is either a relativistic particle beam or an intense laser pulse, excites a highly nonlinear wake in the plasma electron density [8]. The wake consists of a longitudinal train of spherical-like bubbles devoid of plasma electrons that are approximately quasistatic in the frame comoving with the driver. A trailing particle beam can typically be accelerated and focused when injected into the back of the first bubble.

Recent breakthroughs in PBAs have demonstrated its potential wide range of applicability. PBAs are being explored for positron acceleration [9–11]. Two PBA stages driven by laser pulses in capillary discharge plasmas were used to first produce and then accelerate electron beams, at the BELLA Center [12]. Electron beams were split into a two-beam (driver-trailing) configuration to be sent together into 130 cm-long lithium plasma sources leading to wake formation and trailing acceleration up to 9 GeV, at the FACET facility [13]. Also at FACET, experiments showed that the driver-wake energy extraction efficiency could reach over 30% [14]. At the Advanced Wakefield (AWAKE) experiment at CERN, 400 GeV proton beams were used to excite plasma wakes in a m-long rubidium vapor source and accelerate an externally injected trailing electron beam [15]. As future experiments are being designed for and installed at the FACET-II upgrade of the FACET facility, it becomes timely to investigate PBA techniques for improving the quality of the beams delivered to meet the requirements for collider and FEL applications [6].

One of the challenges of current PBA configurations is to produce electron beams that can reach energy spread values as low as competing technologies, i.e., on the order of 0.1%. Electron beams accelerated in PBAs have yet to reach final energy spread values below 1% as is required for collider and FEL applications [14,16–18]. For accelerated beams to have a low energy spread they need to be created and injected with an initially low energy spread and to propagate stably in uniform accelerating fields. The latter takes place when the trailing charge beam loads the wakefields [19]. The operating principle of beam loading relies on longitudinally shaping the beam density profile such that its space-charge fields flatten the, otherwise varying, plasma accelerating wakefield throughout the beam length.

Understanding the correlation between the trailing beam charge shape, in particular its longitudinal density profile, and the associated accelerating wakefields is necessary to determine the criteria for beam loading. An experiment done with a laser driven PBA showed that ionization injection can be used to study the effects of the trailing beam charge in associated accelerating wakefields [17]. Beam-shaping was attempted experimentally for drive particle beams, resulting in beam-loaded decelerating fields and transformer ratios (i.e., ratio between peak decelerating and peak accelerating wakefields experienced by the driver and witness beams, respectively) of about 4.6 [20]. A scheme for shaping and injecting the trailing beam to establish beam loading is still lacking.

In this paper we discuss how the particle beam-induced-ionization injection (B-III) technique can be used to shape and inject trailing beams in PBAs. B-III is an advantageous plasma accelerator technique because it allows self-truncated injection times and production of self-aligned, narrow, high-current beams. Experimental and numerical results have shown that B-III can be used in different realistic PBA scenarios, in particular to create multicolored beams [21], which can be affected by the introduction of an additional inception beam [22,23]. The trailing beams' shapes can be tailored at a micrometer scale by controlling the impurity density profile on a millimeter scale—ionization of which allows the injection of the shaped bunch in the wake. We performed numerical simulations that demonstrated the creation of a shaped trailing beam with 340 pC charge, that reached 900 MeV energy and peak current of 13 kA after propagating less than 3 cm in a plasma. The shaping process that we detail in this paper was suitable for a driver-plasma configuration similar to those that were available at FACET and is an ideal candidate for achieving beam loading in future experiments at the FACET-II facility.

Although the work in this paper demonstrates the possibility of controlling the trailing beam shape via manipulation of the impurity section, the final beam energy spread was on the order of what has already been achieved in PBAs, instead of the desired below 1% range. The reason for this is that the high beam current and space charge fields in the beam-loaded simulations lead to non-linearities and numerical instabilities in the beam region that affect the beam shape and the longitudinal loaded field. Notwithstanding, the positive results of beam shaping discussed in this paper will motivate future work on creating an analytical framework and scaling laws required for shaping trailing beams to reach ideal beam loading in any typical B-III configurations and regimes of operation.

We will begin by explaining how B-III works using an electron driver and a gas of low-ionization-field-threshold (such as H_2—hydrogen), in Sec. II, and how it can produce a trailing beam by addition of a higher-ionization-field-threshold impurity (He—helium), in Sec. III. In Sec. IV we will resort to results from numerical simulations done with particle-in-cell fully relativistic massively parallel code OSIRIS [24,25] to determine the correlation between the driver evolution, plasma bubble, and impurity properties and the injected trailing beam profile. The beam profile required to trigger beam loading is determined in Sec. V. The possible mitigation of the inception beam is discussed in Sec. VI. We are exploring the application of the B-III shaping technique to different driver-plasma configurations, and in particular, to the narrower, shorter and higher current drive beams that are expected to be available at FACET-II. Our promising preliminary results, with final

energy spread as low as 3%, are shown in Sec. VII and highlight the technique's versatility and wide range of applicability. The key advantages and challenges of shaping beams via B-III for beam loading the plasma wakefields are summarized in Sec. VIII.

II. UNMATCHED DRIVER EVOLUTION

In particle beam driven PBAs, the transverse envelope of the driver, σ_r, evolves along the propagation direction, z, according to the betatron equation [26,27]:

$$\frac{d^2\sigma_r}{dz^2} + K_\beta^2\sigma_r(z) = \frac{\epsilon_N^2}{\gamma^2\sigma_r^3(z)}. \quad (1)$$

Where $K_\beta \equiv k_p/\sqrt{2\gamma}$ is the plasma betatron strength factor and $k_p \equiv \sqrt{4\pi e^2 n/m_e c^2}$ is the plasma wavenumber for the effective plasma charge density n in cgs units. ϵ_N and γ are the driver normalized emittance and relativistic Lorentz factor [28]. The driver is matched to the plasma when $K_\beta^2\sigma_r(z) = \frac{\epsilon_N^2}{\gamma^2\sigma_r^3(z)}$ and its envelope remains stationary. It is technically challenging to reach and maintain the matching condition. When the driver is unmatched, it performs betatron oscillations at wavelength $\lambda_\beta = 2\pi/K_\beta$, in which its density and its space charge transverse fields increase as its envelope contracts. At the local minima of σ_r, i.e., where the driver pinches, the fields are maximum. The pinch fields can be used to trigger localized ionization of an impurity gas with ionization field threshold above the initial beam space charge fields.

To illustrate the evolution of an unmatched driver in a plasma, two-dimensional axis-symmetric particle-in-cell (PIC) simulations are done using the fully relativistic and massively parallel PIC code OSIRIS [24,25] and detailed in [23]. The driver parameters were within the range delivered to FACET experiments and are listed in Table I, as well as the plasma and numerical parameters.

Figure 1 shows the transverse electric field of the driver, E_r, and its pinch locations (blue regions), where it is capable of ionizing a neutral He impurity gas (green line), as it propagates through the plasma (blue line). The driver (initial profile illustrated by black line) space charge governs E_r in $\xi \in [60, 200]$ μm, where $\xi = z - ct$ represents the co-moving variable and ct the propagation distance. According to the Ammosov-Delone-Krainov (ADK) model [29] (applied as in [23]), He atoms will be ionized with 10% (100%) probability, by slices surpassing the field threshold of 61 GV/m (73 GV/m). The ionization front defined as the slice with highest ξ value that has E_r above the ionization threshold, evolves along the propagation distance ct. This is because different driver slices experience different decelerating and transverse wakefields, as they travel in different phases of the bubble.

Fields above 166 GV/m would be required to trigger ionization of the second level of 1% of the He atoms. In the driver region, E_r is below 120 GV/m so there is no secondary ionization of He by the driver. At the back of the bubble, approximately $\xi \in [42, 53]$ μm, plasma electrons overshoot the axis in a tight spot leading to E_r over 500 GV/m where He atoms can be fully ionized. The high fields ahead of that region, $\xi \in [53, 75]$ μm, result from the injected beams and can lead to ionization of He atoms and

TABLE I. Control simulation driver, plasma, and numerical parameters for the configuration with long, wide driver (FACET-I).

Driver	Charge (Q_d)	3.2 nC
	Energy (En)	20.4 GeV
	Energy spread (δEn)	0%
	Profile	Bi-Gaussian
	Deviations (σ_z/σ_r)	30/30 μm
	Emittance (ϵ_N)	120 μm
	Particles per cell	4×4
H_2 plasma	Peak density (n_0)	2.5×10^{17} cm^{-3}
	Longitudinal plateau	5 cm
	Up and down-ramps	1 cm
	Transverse profile	Uniform
	Transverse radius	104 μm
	Particles per cell	2×2
	Ions/electrons	Fixed/mobile
	Ionization state	Pre-ionized
PIC grid	Dimensions	255×128 μm^2
	No. of cells	588×360
	Geometry	2D-cylindrical
	Moving window	Applied

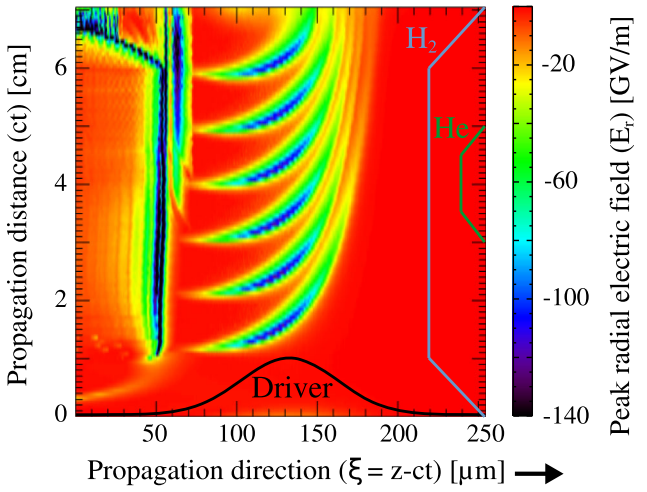

FIG. 1. Color map of the simulation peak radial electric field, E_r, along the co-moving direction $\xi = z - ct$ and propagation distance, ct. Color bar reaches up to -150 GV/m. Blue and green lines illustrate the plasma and He impurity longitudinal density profiles, of the control simulation. Black line shows the driver profile normalized to background plasma density, n_0. The driver propagates from left to right side of the plot.

formation of the inception beam that will be discussed in Secs. III and VI.

III. INJECTION OF THE TRAILING BEAM

To study the shaping process, two simulations are performed: a "control" simulation, where the impurity gas has a density profile composed of a flat-top section that is enveloped by linear up and down ramps, and another with an optimized impurity (He) density profile. The latter will be derived in Sec. V. In the control simulation, a He neutral gas (with an ionization potential of IP = 24.6 eV for its first electron, $Z = 1$) is introduced in the plasma after the bubble structure and wakefields are stable, at $z = 3$ cm as illustrated in Fig. 1 (green line), with the properties described in Table II.

The 2 cm long He section encompassed mainly two betatron pinches of the driver (blue regions of Fig. 1). The pinch region close to $ct \approx 5$ does not lead to significant charge injection because it develops already in the impurity density down-ramp. Thus there were two regions for charge injection, leading to two distinct accelerating distances and trailing beams with separate final energies, but similar density profiles—shapes. For the purpose of this paper, we will focus only on the second, lower-energy injected beam that accelerated for less than 3 cm in the plasma, which will be shaped. The reason for selecting that beam is that it results from ionization after 4.1 cm and mainly within the He flat-top density region. Thus eliminating errors due to changing neutral gas density in our shaping analysis. The final properties of that beam are listed in Table III and its profile is depicted in Fig. 2(b).

The trailing beam shape, i.e., longitudinal density profile, is nearly stable after the He gas section, $ct = 5$ cm. The shape can be approximated by the linear equation expressed in Eq. (2) as a function of the injected relative position ξ_f:

$$dQ/d\xi(\xi_f)[\mathrm{pC}/\mu\mathrm{m}] \approx 120.3 - 1.6\xi_f[\mu\mathrm{m}]. \qquad (2)$$

For simplicity, we neglected the tail beam slices that had $\xi < 65$ μm. The inception beam also shown in Figs. 2(b) and 2(c) (red) results from the B-III of the high current

TABLE II. Control simulation He impurity parameters for the configuration with long, wide driver (FACET-I).

He atoms	Peak density (n_0)	0.01 n_0
	Longitudinal plateau	1 cm
	Up and down-ramps	0.5 cm
	Transverse profile	Uniform
	Transverse radius	104 μm
	Particles per cell	2×2
	Ions/electrons	Fixed/mobile
	Ionization state	Neutral
PIC	Ionization model	ADK

TABLE III. Injected trailing (black) and inception (red) beams charge, Q; current, I; Root-Mean-Square (RMS) energy of the non-centered weighted energy (i.e., $\sqrt{\sum_i q_i En^2 / \sum_i q_i}$ over all beam macro-particles i), En, and energy spread, δ En; and beam longitudinal and transverse standard deviations, σ_z and σ_r; corresponding to the beams plotted in Fig. 2(b) (see [23] for more detail). Results are from the control simulation that uses the longitudinal flat-top plasma profile as shown by green line in Fig. 2(a), and are extrapolated from a total of 20% of all He released electron macroparticles in the simulation box at the end of the run (after they left the plasma).

	Q [pC]	I [kA]	En [GeV]	δEn [%]	σ_z/σ_r [μm]
Beam	99.3	4.5	1.0	5.1	2.8/2.2
Inception	33.2	6.1	1.4	31.3	0.7/1.2

trailing beams injected [22,23]. The space charge fields of the injected beams reach over 61 GV/m within $\xi \in [50, 75]$ and $ct > 3.5$ cm. For that reason they are sufficient to ionize the He atoms and the released electrons can be trapped closer to the back of the bubble, forming the inception beam. This ionization process is continuous, as

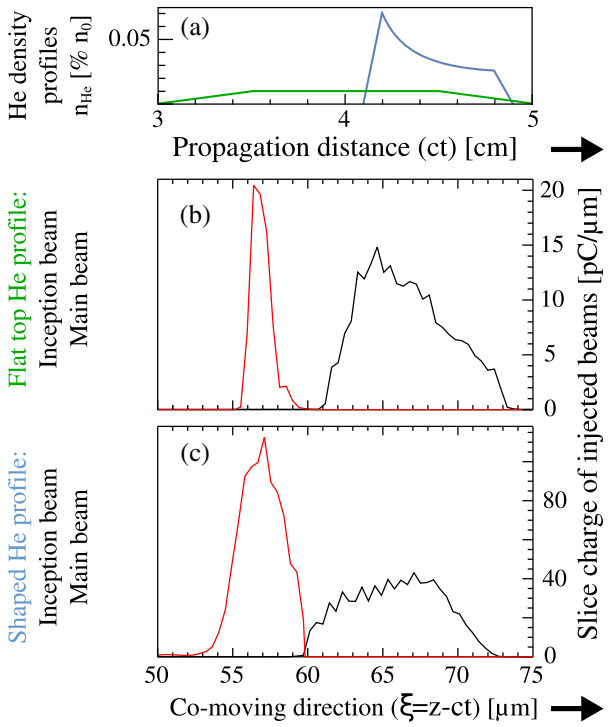

FIG. 2. Plot of the longitudinal He impurity density profile for the simulations with flat-top (control simulation, in green), and tailored density profiles (optimized simulation, in blue). Vertical axis corresponds to the propagation distance, ct. (b) and (c) show the longitudinal slice charge at the end of the two simulations, $ct \approx 7$ cm. The B-III injected main trailing beam is shown in black and the inception beam is shown in red. The slice charge scales in (b) and (c) are different, for clarity. Trailing beam propagation direction is from left to right side of the figure.

opposed to that of the driver, which can only ionize near the pinch location, Fig 1. This results in a large energy spread for the inception beam. In this paper we will address how to shape the trailing beam to reach beam loading, while possibly mitigating the contribution of the high energy spread (33.2%) inception beam.

IV. RELATION BETWEEN IMPURITY AND TRAILING BEAM PROFILES

To correlate the shape of the trailing beam and impurity density, we need to characterize the B-III ionization and injection processes. Ionization by the driver is determined mainly by E_r that leads to 100% probability of ionization in the driver pinch locations. The pinch positions are plotted in Fig. 3 (blue dots) as well as the released electron charge, at each 0.7 mm propagation distance. For a first approximation, we will assume that ionization follows the pinch, which can be fitted by the quadratic function of Eq. (3).

$$\xi_p(ct)[\mu\mathrm{m}] = -1527.9 + 682.9ct[cm] - 69.7ct[cm]^2. \quad (3)$$

He electrons are trapped in the bubble accelerating phase if they are accelerated before transversely escaping the bubble. Analytically this corresponds to the requirement that their initial and trapped normalized effective potential $\Psi = \Phi - \frac{v_z}{c}A_z$, variation verifies the inequality: $\Delta\Psi < -1$ [29]. Where Φ and A are the electromagnetic scalar and vector potentials and v_z is the released electrons velocity. Because ionization can occur at various r positions, it is non-trivial to determine their initial Ψ. The analysis of selected particle trajectories (explained later in Sec. VII) shows that the injection relative position ξ_f, varies approximately linearly with the pinching one ξ_p. Because the trailing beam range is of about $\Delta\xi_f \approx 11.5$ μm, starting at

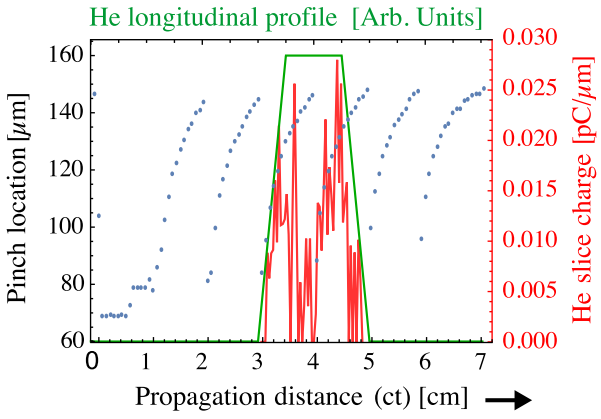

FIG. 3. Plot of the numerical data points for the local minima of the driver envelope (pinch—blue dots) along the propagation distance, ct, for each slice in $\xi = z - ct$, from the control simulation. Red line corresponds to the charge released at the pinch location of each ct position, inside the He neutral gas section. Longitudinal He profile is illustrated by green line.

$\xi_{f0} = 71.2$ μm, and the pinching cycle spans a region of $\Delta\xi_p \approx 40$ μm from its initial value of $\xi_{p0} = 100$ μm, it is possible to write the correlation between the two as Eq. (4).

$$\xi_f(\xi_p)[\mu\mathrm{m}] \approx \xi_{f0} - (\xi_p - \xi_{p0})\frac{\Delta\xi_f}{\Delta\xi_p} = 71.2 - 0.3(\xi_p[\mu\mathrm{m}] - 100). \quad (4)$$

Combining Eqs. (2) to (4) allows us to write the deposited slice charge density as a function of the location of the pinch, which will be necessary to determine the tailored He impurity density profile required to shape the beam for beam loading.

V. TRAILING BEAM SHAPED FOR BEAM LOADING

Beam loading manifests itself as the flattening of the plasma longitudinal wakefield along the beam length due to the energy extraction by the trailing beam. We will apply the theory of beam loading of the standard nonlinear blowout regime as explained in [19]. Its validity is restricted to plasma based accelerators (PBA) blowout regimes with plasma bubble radius $R_b \gg 1$, even though the case considered here corresponds to $R_b \approx 1$. The trailing beam used to numerically benchmark the theoretical predictions had a trapezoidal longitudinal density profile and was radially uniform. B-III does not produce radially uniform beams, in particular because the injected beam also performs betatron oscillations. The model can still be used as a first step toward computing the beam shape required to beam load the wakefields.

According to [19], to match the beam space charge fields with the wakefield, the wakefield information at the head of the beam, ξ_{f0} is required. We resorted to a simulation with the same setup as the one explored this far, but with negligible (only 0.05%) impurity concentration to study the longitudinal accelerating field in the region of beam injection throughout its acceleration process. At $ct \approx 5$ cm and $\xi = \xi_{f0}$, the longitudinal wakefield was about $E_s = -40.1$ GV/m at the bubble sheath, i.e., at $r = r_s = 19.4$ μm. The peak bubble sheath radius observed in this simulation is $R_b = 26.7$ μm. The shape that the trailing beam needs to reach beam loading is then given by (5), which is plotted in Fig. 4 and followed the analysis done in [19], where dimensions were normalized to the plasma skin depth, $1/k_p$, densities to the plasma peak background density, n_0, and fields to the cold wave-breaking limit, $E_{WB} = m_e c^2 k_p/e$.

$$n_s(\xi, r)[N.U] = \exp\left(-\frac{r^2}{2\sigma_{rHe}^2}\right) F\sqrt{E_s^4 + R_b^4/16} - E_s(\xi[N.U] - \xi_{f0}). \quad (5)$$

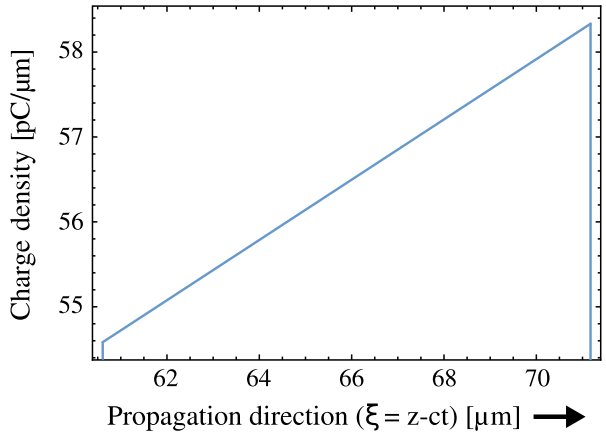

FIG. 4. Plot of the longitudinal trailing beam slice charge density required to beam load the wakefields, Eq. (5), as a function of the injected location in the comoving frame, $\xi = z - ct$.

The constant factor $F = 0.01 n_0/\sigma_{rHe}^2$ includes the two corrections required to estimate the total injected charge for ideal beam loading. The first correction results from the charge injected in the control simulation being proportional to the concentration of the He impurity, which was $n_{He} = 0.01 n_0$ [23]. The second correction comes from a first order approximation of the injected beam transverse profile by a Gaussian fit of standard deviation σ_{rHe}^2, with value shown in Table III for the control simulation.

Note that the required profile for beam loading has a slice charge density slope of opposite sign as that resulting from B-III with the flat-top density profile, Fig. 2(b) (black line). To determine the optimized impurity longitudinal profile, we first match the desired injected beam shape for beam loading [Eq. (5)] to the result of the beam shape from the control simulation with a flat-top impurity [Eq. (2)] as a function of injected slice. We then use the knowledge of the correlation between the injected slice and the ionization slice [(4)], which is related to the pinch longitudinal location [Eq. (3)], to compute the optimized impurity longitudinal profile illustrated in Fig. 2(a) (blue line) and given by Eq. (6) also in normalized units.

$$n_s(z)[N.U] = \frac{-6.1 \times 10^4 + 20.1z - 0.021z^2}{2.05 \times 10^7 - 9.2 \times 10^3 z + z^2} \quad (6)$$

That impurity profile was used in an optimized simulation done with the same driver-plasma configuration as the controlled simulation, which was described in Sec. II. The optimized impurity lead to the injection of one trailing beam (black) and one inception beam (red line) with final profiles shown in Fig. 2(c). As expected the trailing beam shape has now a reversed sign slope, indicating successful shaping of the trailing beam in a μm scale, via the use of the cm scale tailored impurity density profile in a B-III scheme.

TABLE IV. Injected trailing (black) and inception (red) beams charge, Q; current, I; Root-Mean-Square (RMS), En, and energy spread, δ En; and beam longitudinal and transverse standard deviations, σ_z and σ_r; from the simulation with the He profile given by Eq. (6), which is plotted in Fig. 2(a) in blue. Results extrapolated from all He released electron macroparticles in the simulation box at the end of the run (after they left the plasma).

	Q [pC]	I [kA]	En [GeV]	δEn [%]	σ_z/σ_r [μm]
Beam	340.5	12.9	0.9	11.1	2.9/3.2
Inception	403.5	33.7	0.4	47.9	1.6/2.8

The properties of both injected beams are listed in Table IV.

VI. INCEPTION BEAM MITIGATION

As shown in [22,23], the inception beam is created due to the high space charge fields of the main injected beams. Those fields ionize the He atoms and the electrons released within the region of the main injected beams can be trapped and accelerated closer to the back of the bubble, forming the inception beam. The inception beam created in the optimized simulation (with the tailored He profile) is formed in the same way as that of the control (flat-top) simulation, but, because of the higher trailing beam current in the first, more electrons were injected into the inception beam. In the optimized case, the inception beam energy spread is about 48% and it is attached to the main injected beam. For that reason the inception beam is jeopardizing the overall quality of the total injected charge in this simulation.

As a result of the inception beam high current, however, its space charge field over compensates the accelerating field, leading to the significant deceleration of its electrons. Consequently, by enlarging the distance of acceleration for both beams (i.e., by using a longer H_2 plasma) the inception beam can gradually distance itself in energy from the trailing beam, which is accelerating in loaded wakefields. In this way, by using, for example, a magnet to spread the final total injected charge it will be possible to fully remove the inception beam and use the higher quality trailing beam for desired applications.

The trailing beam higher energy spread, in the optimized simulation, results from its high current exciting nonlinear space charge fields that in turn disrupt the longitudinal field. For that reason, the beam profile shows significant irregularities between consecutive longitudinal cells. This effect compromised the beam's ability to beam load the wakefields. The final energy spread, although controlled due to the trailing beam's shape, is not ideal. We conducted a set of identical simulations, but with increased longitudinal resolution and found that it strongly affects the fields in the beam location, the beams final properties and the inception beams generated. The detailed investigation

TABLE V. Control simulations scan driver, plasma and numerical parameters for the configuration with short, narrow drivers (FACET-II).

Driver	Charge (Q_d)	0.8, 0.82, 0.85, 1 nC
	Energy (En)	10 GeV
	Energy spread (δEn)	0%
	Profile	Bi-Gaussian
	Deviations (σ_z)	20 μm
	Deviations (σ_r)	16 μm
	Emittance (ϵ_N)	0
	Particles per cell	2×2
H_2 plasma	Peak density (n_0)	2.7, 5.4×10^{16} cm^{-3}
	Longitudinal plateau	5 cm
	Up and down-ramps	0.5 cm
	Transverse profile	Uniform
	Transverse radius	125 μm
	Particles per cell	2×2
	Ions/electrons	Fixed/mobile
	Ionization state	Pre-ionized
PIC grid	Dimensions	217×128 μm^2
	No. of cells	2465×840
	Geometry	2D-cylindrical
	Moving window	Applied

and mitigation of this numerical noise effect will be a subject of future work.

VII. SHAPED BEAM USING FACET-II DRIVER PARAMETERS

The FACET-II facility will deliver narrower, shorter and higher-current drive beams than those explored at FACET. Hence, the previous results of the trailing beam shaping via B-III with beam parameters available at FACET, motivated our investigation of its applicability to FACET-II drive beams. To study those configurations we performed additional simulations with OSIRIS according to the parameters listed in Table V.

A He neutral gas was introduced, with parameters as described in Table VI, in the plasma within the region where the driver space charge fields led to its ionization,

TABLE VI. Control simulations scan He impurity parameters for the configuration with short, narrow drivers (FACET-II).

He atoms	Peak density (n_0)	0.5 n_0
	Longitudinal plateau	0.5 cm
	Up and down-ramps	0.1 cm
	Transverse profile	Uniform
	Transverse radius	125 μm
	Particles per cell	2×2
	Ions/electrons	Fixed/mobile
	Ionization state	Neutral
PIC	Ionization model	ADK

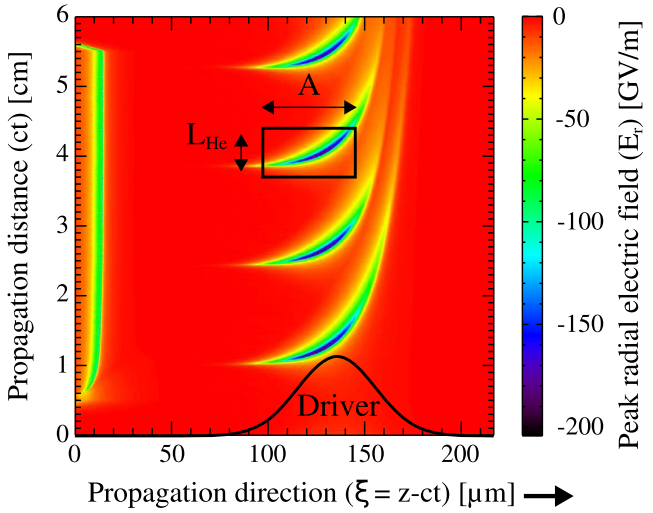

FIG. 5. Color map of the simulation peak radial electric field along the comoving direction $\xi = z - ct$ and propagation distance, ct. Black solid line shows the beam profile normalized to background plasma density, n_0. The black box delimits the region of $\xi \in [100, 150]$ μm where the field reaches 63 GV/m for the interval L_{He} and where He is present, i.e., for $ct \in [3.7, 4.4]$ cm. The driver propagates from left to right side of the plot.

$ct \in [3.7, 4.4]$ cm, [black box of Fig. 5(a)]. The longitudinal profile is depicted in Fig. 7(a) (green line). The resulting injected and accelerated beams profiles are shown in Fig. 6 and the final properties for the 0.8 and 1 nC driver charge cases listed in Table VII. When the driver charge is lower, only the pinch closest to its core slice is capable of ionizing He atoms. Only for the driver with 1 nC charge do the slices closer to its tail, which have

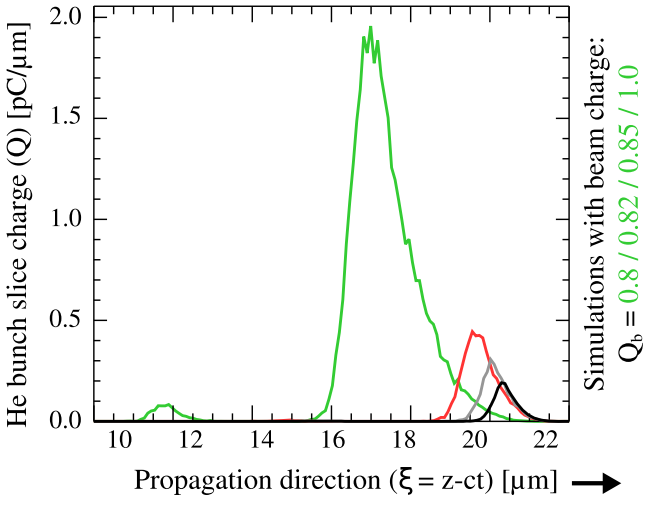

FIG. 6. Plot of the slice charge longitudinal density profile of the trailing beams injected via B-III near the back of the bubble at the end of the simulations, $ct = 6$ cm, performed with driver charges of 0.8, 0.82, 0.85, and 1 nC. Longitudinal axis corresponds to the comoving variable, $\xi = z - ct$, and the propagation direction is from left to right side of the plot.

TABLE VII. Injected beam charge, Q; current, I; root-mean-square (RMS) energy, En, and energy spread, δ En; and beam longitudinal and transverse standard deviations, σ_z and σ_r; from the simulations with flat-top plasma profiles and $Q_d = 0.8$ and 1 nC driver charges.

Q_d [nC]	Q [pC]	I [A]	En [GeV]	δEn [%]	σ_z/σ_r [μm]
0.8	0.1	57	0.42	1.3%	0.3/1.8
1.0	3.2	590	0.45	2.9%	0.8/2.6

higher trapping efficiency, ionize He atoms. For that reason its profile is longer.

Even with the flat-top plasma profile, i.e., without using a tailored impurity, the injected beam in this setup is so narrow that its energy spread is as low as 1.3%. This suggests that by correctly shaping the beam for beam loading, values comparable to standard accelerator technologies could be reached. There is, however, a trade-off between the low energy spread and the amount of charge injected which is too low for possible FEL and collider applications in that case.

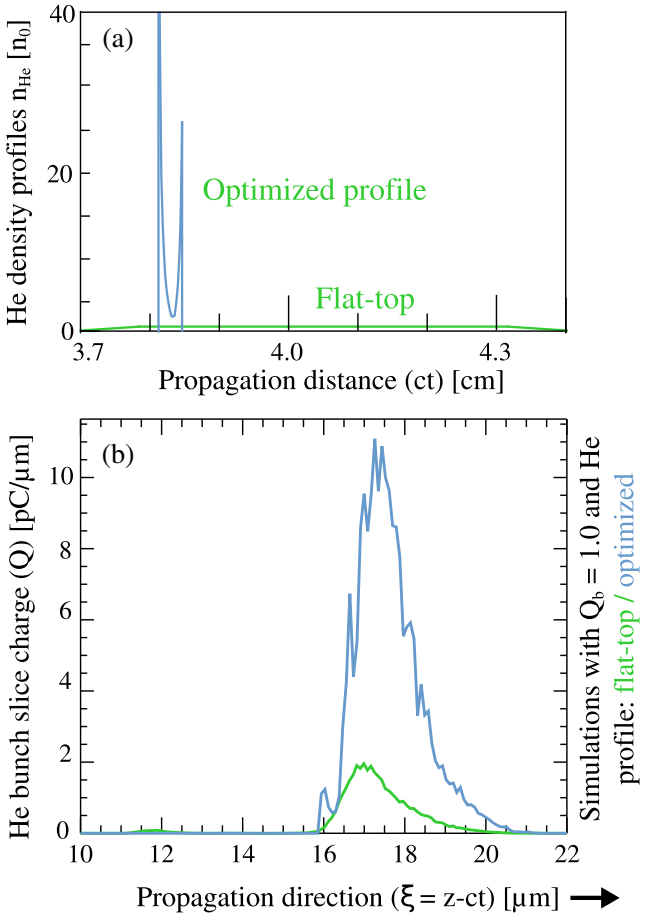

FIG. 7. (a) Illustration of the longitudinal profiles of the He impurity concentration for the simulation done using a flat-top and ramps profile (green) and for the simulation done with the optimized profile (blue). (b) Plot of the slice charge longitudinal density profile of the trailing beams injected via B-III near the back of the bubble at the end of the simulations, $ct = 6$ cm, performed with driver charges of 1 nC and flat-top (green) and optimized profiles (blue). Longitudinal axis corresponds to the co-moving variable, $\xi = z - ct$, and the propagation direction is from left to right side of the plot.

In the configuration where the driver has 1 nC more charge was injected. For that reason that driver configuration is the one chosen for testing the B-III shaping technique discussed in the previous sections of this paper. In the more narrow, tighter drive beam case, shaping was more challenging because the narrower injected beam required much higher resolution for the accurate control of its shape. The resolution in the propagation distance, i.e., of recorded datasets, is also relevant in these scenarios. The ionization and injection occurs at a much shorter time frame than it did for the case explored in the previous sections.

Our preliminary shaping studies have already shown the possibility of injecting single trailing beams of high charge and low energy spread using optimized He longitudinal profiles. The simulation with driver charge of 1 nC and flat-top plasma profile, with parameters described in Tables V and VI and impurity profile shown in Fig. 7(a) (green line), resulted in the injection of the beam with slice charge profile plotted in Fig. 7(b) (green line) and properties as listed in Table VII (bottom row). That simulation was used as the control for a similar analysis as that described in Secs. IV and V, with which we determined the optimized longitudinal impurity profile required to beam load the wakefields. That optimized profile is plotted in Fig. 7(a) (blue line) and with its single shaped beam was injected with: 17.6 pC; the slice charge profile shown in Fig. 7(b) (blue line) and a distribution of 0.8 and 2.5 standard deviations longitudinally and transversely. By tailoring the impurity section it was possible to inject higher charge into a beam with only 3.1% energy spread.

The injected beams energy spread registered for the short and narrow driver (FACET-II) configurations was lower than those registered for the longer and wider driver (FACET). That is because, due to the different beam and plasma properties, in the latter case the beam encompassed the full length of the bubble and a long range of its slices (when compared to the bubble size) was able to ionize and inject electrons into the beams. For that reason the injected beams were longer and experienced a wider range of accelerating wakefields, leading to higher energy spread.

For the same configuration, the analysis of 500 randomly selected injected electron trajectories also allowed us to confirm the validity of the approximation of linear dependency of ξ_f in the ionization location [which in Eq. (4) we approximated by the pinch location, ξ_p] also in the B-III configuration driven by the narrower and shorter drive beam, as can be seen in Fig. 8.

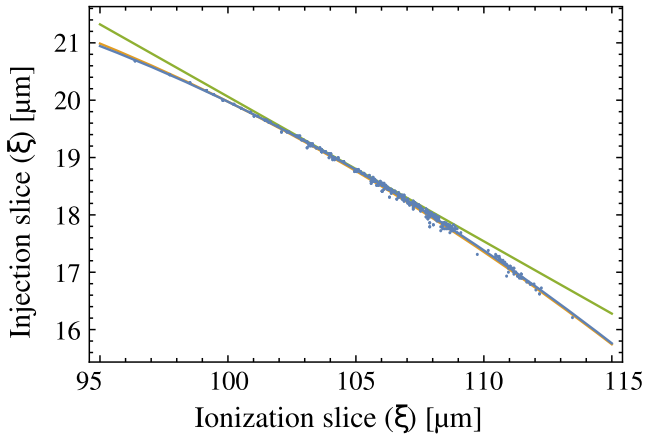

FIG. 8. Plot of the injection relative location as a function of the ionization position of 500 selected electrons represented by the dots. Linear and quadratic fits to those electrons positions are shown by the green and blue lines. Yellow line is similar to blue line and is the result of the quadratic fit done with the weight information of each macroparticle (which depends on the probability of ionization when that particle was created). Propagation direction is from left to right side of the plot.

VIII. CONCLUSIONS AND FUTURE DIRECTION

This work shows that the beam induced ionization injection (B-III) technique can be used to shape and inject trailing beams capable of beam loading plasma wakefields. Through controlling the gas impurity longitudinal density profile at a millimeter scale, it is possible to shape the injected beams profile at a μm scale. Numerical simulations performed with a realistic driver and plasma configuration led to the creation of a 340 pC, 13 kA, and 3 μm long electron beam, via B-III, which was accelerated to 900 MeV in less than 3 cm of plasma. That beam was shaped to beam load the longitudinal wakefields (i.e., to produce uniform accelerating fields for itself) to reduce its final energy spread. In particular, the simulations done with driver parameters possible to be delivered to FACET-II allowed the generation of un-shaped beams with energy spread values as low as 1.3% and charge of 0.1 pC. Preliminary results showed that by shaping the beam it was possible to increase the charge injected in it to 3.2 pC, resulting in a final energy spread of 2.9%. These exciting results are a promising step forward in the direction of establishing high accelerating gradient plasma based configurations to deliver low energy spread beams, by reaching the conditions for beam loading.

To determine the robustness of the results found with our two-dimensional cylindrical geometry simulations done with the OSIRIS, it will be important to solve the numerical noise effects and useful to conduct full three dimensional simulations. Additional work is required to generalize the characteristics discussed in this paper to configurations where driver and plasma can be asymmetric, irregular, and misaligned. The next step in characterizing the B-III shaping technique is to derive its analytical framework and scaling-laws. It was shown in [30] that by adding an external transverse magnetic field to our configuration, the criteria for ideal beam loading were relaxed allowing more charge in the tailored injected beam. In the future, it will be interesting to test if the conclusions are valid for our particle beam driven PBA configuration.

ACKNOWLEDGMENTS

The authors acknowledge funding from the resources of the National Energy Research Scientific Computing Center, a DOE Office of Science User Facility supported by the Office of Science of the U.S. Department of Energy under Contract No. DE-AC02-05CH11231, and of the SEAWULF computer cluster at Stony Brook University. The OSIRIS 4.0 framework was provided by the OSIRIS Consortium, consisting of UCLA (CA, United Sates) and IST (Lisbon, Portugal), supported by National Science Foundation under Contract No. ACI-1339893.

[1] W. Henning and C. Shank, Accelerators for America's future report, ECE Report No. AL944 (U.S. Department of Energy, Washington, DC, 2010).

[2] Advanced Accelerator Development Strategy Report, Advanced Accelerator Concepts Research Roadmap Workshop, Technical Report (U.S. Department of Energy Office of Science, Washington, DC, 2016).

[3] S.-H. Kim, Protection of accelerator hardware: Rf systems, CERN Yellow Reports **2**, 361 (2016).

[4] Accelerator Division III Tetsuo ABE, Minuscule gremlins cause vacuum breakdown in radio-frequency accelerating cavities, https://www2.kek.jp/accl/eng/topics/topics190122.html (2019), accessed: 2019-04-9.

[5] I. Blumenfeld, C. E. Clayton, F.-J. Decker, M. J. Hogan, C. Huang, R. Ischebeck, R. Iverson, C. Joshi, T. Katsouleas, N. Kirby, W. Lu, K. A. Marsh, W. B. Mori, P. Muggli, E. Oz, R. H. Siemann, D. Walz, and M. Zhou, Energy doubling of 42 Gev electrons in a metre-scale plasma wakefield accelerator, Nature (London) **445**, 741 (2007).

[6] C. Joshi, E. Adli, W. An, C. E. Clayton, S. Corde, S. Gessner, M. J. Hogan, M. Litos, W. Lu, K. A. Marsh, W. B. Mori, N. Vafaei-Najafabadi, B. O'shea, Xinlu Xu, G. White, and V Yakimenko, Plasma wakefield acceleration experiments at FACET II, Plasma Phys. Controlled Fusion **60**, 034001 (2018).

[7] T. Tajima and J. M. Dawson, Laser Electron Accelerator, Phys. Rev. Lett. **43**, 267 (1979).

[8] W. Lu, C. Huang, M. Zhou, W. B. Mori, and T. Katsouleas, Nonlinear Theory for Relativistic Plasma Wakefields in the Blowout Regime, Phys. Rev. Lett. **96**, 165002 (2006).

[9] A. Alejo, R. Walczak, and G. Sarri, Laser-driven high-quality positron sources as possible injectors for plasma-based accelerators, Sci. Rep. **9**, 5279 (2019).

[10] J. Vieira and J. T. Mendonça, Nonlinear Laser Driven Donut Wakefields for Positron and Electron Acceleration, Phys. Rev. Lett. **112**, 215001 (2014).

[11] L. D. Amorim, J. Vieira, R. A. Fonseca, and L. O. Silva, Positron plasma wakefield acceleration in a self-driven hollow channel, AIP Conf. Proc. **1777**, 070001 (2016).

[12] S. Steinke, J. van Tilborg, C. Benedetti, C. G. R. Geddes, C. B. Schroeder, J. Daniels, K. K. Swanson, A. J. Gonsalves, K. Nakamura, N. H. Matlis, B. H. Shaw, E. Esarey, and W. P. Leemans, Multistage coupling of independent laser-plasma accelerators, Nature (London) **530**, 190 (2016).

[13] M. Litos, E. Adli, J. M. Allen, W. An, C. I. Clarke, S. Corde, C. E. Clayton, J. Frederico, S. J. Gessner, S. Z. Green, M. J. Hogan, C. Joshi, W. Lu, K. A. Marsh, W. B. Mori, M. Schmeltz, N. Vafaei-Najafabadi, and V. Yakimenko, 9 GeV energy gain in a beam-driven plasma wakefield accelerator, Plasma Phys. Controlled Fusion **58**, 034017 (2016).

[14] M. Litos *et al.*, High-efficiency acceleration of an electron beam in a plasma wakefield accelerator, Nature (London) **515**, 92 (2014).

[15] E. Adli *et al.*, Acceleration of electrons in the plasma wakefield of a proton bunch, Nature (London) **561**, 363 (2018).

[16] M. Hansson, B. Aurand, H. Ekerfelt, A. Persson, and O. Lundh, Injection of electrons by colliding laser pulses in a laser wakefield accelerator, Nucl. Instrum. Methods Phys. Res., Sect. A **829**, 99 (2016).

[17] J. P. Couperus, R. Pausch, A. Köhler, O. Zarini, J. M. Krämer, M. Garten, A. Huebl, R. Gebhardt, U. Helbig, S. Bock, K. Zeil, A. Debus, M. Bussmann, U. Schramm, and A. Irman, Demonstration of a beam loaded nanocoulomb-class laser wakefield accelerator, Nat. Commun. **8**, 487 (2017).

[18] Y. Li, G. Xia, K. V. Lotov, A. P. Sosedkin, K. Hanahoe, and O. Mete-Apsimon, High-quality electron beam generation in a proton-driven hollow plasma wakefield accelerator, Phys. Rev. Accel. Beams **20**, 101301 (2017).

[19] M. Tzoufras, W. Lu, F. S. Tsung, C. Huang, W. B. Mori, T. Katsouleas, J. Vieira, R. A. Fonseca, and L. O. Silva, Beam Loading in the Nonlinear Regime of Plasma-Based Acceleration, Phys. Rev. Lett. **101**, 145002 (2008).

[20] Gregor Loisch *et al.*, Observation of High Transformer Ratio Plasma Wakefield Acceleration, Phys. Rev. Lett. **121**, 064801 (2018).

[21] N. Vafaei-Najafabadi *et al.*, Producing multi-colored bunches through beam-induced ionization injection in PWFA, Phil. Trans. R. Soc. A **377** (2019).

[22] L. D. Amorim and N. Vafaei-Najafabadi, Narrow "inception" beams generated in facet beam-driven wakefield accelerator setups, *IEEE Advanced Accelerator Concepts Workshop (AAC), Breckenridge, CO, USA* (2018), pp. 1–5, https://doi.org/10.1109/AAC.2018.8659382.

[23] L. D. Amorim and N. Vafaei-Najafabadi, Ionization injection of "inception" beams in plasma wakefield accelerators, Plasma Phys. Control. Fusion **61**, 105015 (2019).

[24] R. A. Fonseca, S. F. Martins, L. O. Silva, J. W. Tonge, F. S. Tsung, and W. B. Mori, One-to-one direct modeling of experiments and astrophysical scenarios: pushing the envelope on kinetic plasma simulations, Plasma Phys. Controlled Fusion **50**, 124034 (2008).

[25] R. A. Fonseca, L. O. Silva, F. S. Tsung, V. K. Decyk, W. Lu, C. Ren, W. B. Mori, S. Deng, S. Lee, T. Katsouleas, and J. C. Adam, Osiris: A three-dimensional, fully relativistic particle in cell code for modeling plasma based accelerators, in *Computational Science—ICCS 2002*, edited by P. M. A. Sloot, A. G. Hoekstra, C. J. Kenneth Tan, and J. J. Dongarra (Springer Berlin Heidelberg, Berlin, Heidelberg, 2002), pp. 342–351.

[26] E. Esarey, B. A. Shadwick, P. Catravas, and W. P. Leemans, Synchrotron radiation from electron beams in plasma-focusing channels, Phys. Rev. E **65**, 056505 (2002).

[27] C. E. Clayton *et al.*, Transverse Envelope Dynamics of a 28.5-Gev Electron Beam in a Long Plasma, Phys. Rev. Lett. **88**, 154801 (2002).

[28] Unless specified otherwise, variables and equations are presented in the CGS unit system throughout this paper.

[29] A. Pak, K. A. Marsh, S. F. Martins, W. Lu, W. B. Mori, and C. Joshi, Injection and Trapping of Tunnel-Ionized Electrons into Laser-Produced Wakes, Phys. Rev. Lett. **104**, 025003 (2010).

[30] Q. Zhao, S. M. Weng, Z. M. Sheng, M. Chen, G. B. Zhang, W. B. Mori, B. Hidding, D. A. Jaroszynski, and J. Zhang, Ionization injection in a laser wakefield accelerator subject to a transverse magnetic field, New J. Phys. **20**, 063031 (2018).